Stochastic dynamics of micron-scale doubly clamped beams in a viscous fluid

M. M. Villa and M. R. Paul*
Department of Mechanical Engineering, Virginia Polytechnic Institute and State University, Blacksburg, Virginia 24061, USA
(Received 25 November 2008; published 28 May 2009)

We study the stochastic dynamics of doubly clamped micron-scale beams in a viscous fluid driven by Brownian motion. We use a thermodynamic approach to compute the equilibrium fluctuations in beam displacement that requires only deterministic calculations. From calculations of the autocorrelations and noise spectra we quantify the beam dynamics by the quality factor and resonant frequency of the fundamental flexural mode over a wide range of experimentally accessible geometries. We consider beams with uniform rectangular cross section and explore the increased quality factor and resonant frequency as a baseline geometry is varied by increasing the width, increasing the thickness, and decreasing the length. The quality factor is nearly doubled by tripling either the width or the height of the beam. Much larger improvements are found by decreasing the beam length, however this is limited by the appearance of additional modes of fluid dissipation. Overall, the stochastic dynamics of the wider and thicker beams are well predicted by a two-dimensional approximate theory beyond what may be expected based upon the underlying assumptions, whereas the shorter beams require a more detailed analysis.

DOI: 10.1103/PhysRevE.79.056314 PACS number(s): 47.61.Fg, 83.10.Mj, 85.85.+j

I. INTRODUCTION

There is a growing need for fast and sensitive micron and nanoscale sensors and actuators that operate in viscous fluid environments. Many important technologies are based upon the dynamics of small elastic beams in fluid [1–4]. If an elastic beam is uniformly reduced in size it will become both softer (the equivalent spring constant is reduced) and faster (the fundamental frequency of oscillation increases). This advantageous trend is often exploited [4]. However, in a fluid environment the relative magnitude of viscous forces to inertial forces becomes large resulting in a dramatic reduction in the quality factor and resonant frequency of the fundamental mode of oscillation. For example, the dynamics of a nanoscale cantilever in water can be overdamped [5]. Several approaches have been proposed to overcome this difficulty including the use of the higher order beam modes [1,6–10], nonlinear feedback control strategies for the external drive [11,12], by varying the cross-sectional geometry of long-thin cantilevers that are driven externally [10], and by embedding the fluid inside the cantilever while it oscillates in vacuum [13]. However, these approaches can be difficult to implement in practice and often require sophisticated measurements and control electronics. In addition, for the strongly damped dynamics under consideration here the mode of actuation directly affects the resulting quality factor and resonant frequency (cf. [14]). In many applications a simpler tactic is desirable to overcome the strong viscous damping. In this paper we explore the variation in beam dynamics as a function of its geometry. In particular, we quantify the stochastic dynamics of doubly clamped beams with rectangular cross section for a wide range of sizes and geometries including short and wide beams that are not well described by available analytical theory. Using numerical simulations for the precise conditions of experiment we quantify the Brownian driven dynamics of micron-scale beams in fluid and explore the physical origins of the fluid dissipation. These results determine the effectiveness of tailoring the beam geometry to overcome the strong viscous damping.

We calculate the stochastic dynamics of the doubly clamped beams [see Fig. 1] using the thermodynamic approach discussed in detail in Refs. [5,14]. The approach requires only a single deterministic calculation of the fluid dissipation that is used to compute the stochastic beam displacement via the fluctuation-dissipation theorem. For a doubly clamped beam the deterministic calculation is the ring down of the beam due to the removal of a step point force applied to the center of the beam. We emphasize that the only assumptions in this result are that of classical dynamics and small deflections. Using three-dimensional, time-dependent, finite element simulations for the precise geometries of interest the stochastic dynamics is computed. In particular, we calculate the autocorrelations and noise spectra of equilibrium fluctuations in the beam displacement. The

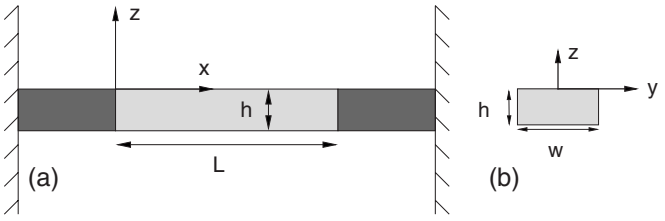

FIG. 1. A schematic of a doubly clamped beam used in the numerical simulations with length L, width w, and height h with uniform rectangular cross section. (a) The x-z plane of the beam in fluid. The beam is supported by a rigid support of width w on each side for the short-wide geometries to minimize the effects of the bounding side walls. The beam is light gray and the two rigid supports are darker gray. (b) The y-z plane of the beam illustrating the rectangular cross section. In our simulations the beam is immersed in room-temperature water and we compute the stochastic dynamics of the fundamental flexural mode driven by Brownian motion. In the following figures the vertical displacement of the beam at $x=L/2$ is referred to as $z_1(t)$ for thermally induced fluctuations and $Z_1(t)$ for the deterministic ring-down simulations.

*mrp@vt.edu

basic approach has been validated both against analytics and experimental measurement [5,14–17] and also used to study the fluid-coupled motion of two atomic force microscope cantilevers [18] and two nanoscale cantilevers [5,14].

II. DISCUSSION

In many situations of technological and scientific interest, such as atomic force microscopy, the elastic beams are long and thin $L \gg w \gg h$ where L is the length, w is the width, and h is height of the beam. The fluid-solid interaction problem describing the motion of a waving beam in fluid is very difficult with analytical solutions available only under idealized conditions such as simple beam geometries and for small deflections [19–22]. In the limit of small beam displacements, a two-dimensional approximation for the fluid flow over the beam is often used to determine the force interactions with an Euler-Bernoulli beam. This approach has been very successful in predicting the resulting beam dynamics in a viscous fluid [20]. Furthermore, it has been shown that replacing the rectangular beam cross section with that of a cylinder of diameter equal to the width w yields small errors on the order of several percent [19]. The flow field generated by an oscillating cylinder is well known as well as the forces acting on the surface of the cylinder [23,24]. These approximations have led to insightful analytical expressions describing the stochastic dynamics of beams in fluid [5,20]. However, the validity and accuracy of these expressions remain unclear for the finite beam geometries often used in experiment.

A. Analytical approach

In the limit of a long and thin beam, small displacements, and using the two-dimensional approximation of an oscillating cylinder for the fluid flow, the noise spectrum of equilibrium fluctuations in displacement of the beam measured at $x=L/2$ for the fundamental mode is given by [5]

$$G(\omega) = \frac{4k_BT}{k}\frac{1}{\omega_0}\frac{T_0\tilde{\omega}\Gamma_i(R_0\tilde{\omega})}{[\{1-\tilde{\omega}^2[1+T_0\Gamma_r(R_0\tilde{\omega})]\}^2+[\tilde{\omega}^2T_0\Gamma_i(R_0\tilde{\omega})]^2]}, \quad (1)$$

where ω is the frequency of oscillation, $\tilde{\omega}=\omega/\omega_0$ is the reduced frequency, ω_0 is the resonant frequency of the fundamental mode in vacuum, R_0 is the frequency parameter evaluated at ω_0, $\Gamma(\omega)$ is the hydrodynamic function, T_0 is the mass loading parameter, k_B is Boltzmann's constant, T is the temperature, and k is the spring constant for the fundamental mode. The frequency parameter is

$$R_0 = \frac{\omega_0 w^2}{4\nu}, \quad (2)$$

and is a frequency based Reynolds number representing the ratio of local inertia to viscous forces where ν is the kinematic viscosity of the fluid. In our notation, the frequency parameter R is evaluated at arbitrary frequency ω, and R_f is evaluated at ω_f. The mass loading parameter is

$$T_0 = \frac{\pi}{4}\frac{\rho_f w}{\rho_b h} \quad (3)$$

and represents the ratio of the mass of a cylinder of fluid with radius $w/2$ to the actual mass of the beam where ρ_f is the density of the fluid, and ρ_b is the density of the beam. The hydrodynamic function for an oscillating cylinder in a viscous fluid is given by [23,24]

$$\Gamma(\omega) = 1 + \frac{4iK_1(-i\sqrt{iR_0\tilde{\omega}})}{\sqrt{iR_0\tilde{\omega}}K_0(-i\sqrt{iR_0\tilde{\omega}})}, \quad (4)$$

where K_1 and K_0 are Bessel functions, Γ_r and Γ_i are the real and imaginary parts of Γ, respectively, and $i=\sqrt{-1}$.

The dynamics of a beam in fluid is not precisely equivalent to that of a damped simple harmonic oscillator. For example, both the mass and damping are frequency dependent. The mass of the entrained fluid plus the mass of the beam is

$$m_f(\omega) = m_e[1+T_0\Gamma_r(R_0\tilde{\omega})], \quad (5)$$

where $m_e=\alpha m_b$ is the equivalent mass of the beam such that the kinetic energy of this mass is equal to that of the fundamental mode and $m_b=\rho_b Lwh$ is the mass of the beam. For the fundamental flexural mode of a doubly clamped beam $\alpha=0.396$. The viscous damping is

$$\gamma_f(\omega) = m_{cyl,e}\omega\Gamma_i(R_0\tilde{\omega}), \quad (6)$$

where $m_{cyl,e}=\alpha m_{cyl}$ is the equivalent mass of a cylinder of fluid with diameter equal to w. As the frequency of oscillation increases the magnitude of m_f decreases and the magnitude of γ_f increases.

The simple harmonic-oscillator approximation is convenient to define commonly used diagnostics such as the quality factor Q and resonant frequency of the beam in fluid ω_f. As a result of the frequency-dependent mass and damping, the fundamental peak of the noise spectra is not well approximated as a Lorentzian for these strongly damped oscillators and care must be taken when determining Q and ω_f. The resonant frequency in fluid ω_f will be defined to be the frequency which maximizes the noise spectrum in Eq. (1). The quality factor Q is then defined as the ratio of energy stored by the potential and kinetic energy of the beam and fluid to the energy dissipated by viscosity per oscillation when evaluated at ω_f. This yields

$$Q \approx \frac{m_f(\omega_f)\omega_f}{\gamma_f(\omega_f)} = \frac{T_0^{-1}+\Gamma_r(R_0\tilde{\omega}_f)}{\Gamma_i(R_0\tilde{\omega}_f)}. \quad (7)$$

Given values of the nondimensional parameters R_0 and T_0, Eqs. (1) and (7) directly yield the analytical predictions for ω_f and Q. The variation in Q and ω_f with R_0 and T_0 are shown in Fig. 2 over a large range of parameters. The quality factor increases significantly as the frequency of oscillation is increased and also increases as the mass loading decreases. The resonant frequency of the beam when placed in fluid, ω_f/ω_0, also increases with frequency of oscillation and with a reduction in mass loading. The increase of ω_f/ω_0 with respect to R_0 is very rapid for $R_0 \lesssim 20$ with only small changes for higher frequencies, while the dependence upon T_0 results in a nearly uniform increase over the range shown.

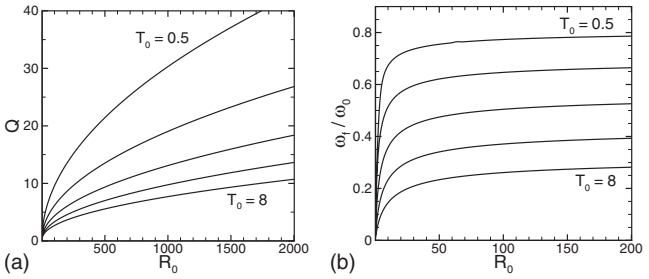

FIG. 2. (a) The predicted variation of the quality factor Q for the stochastic displacement of a beam immersed in a viscous fluid with respect to the nondimensional frequency parameter R_0 and mass loading parameter T_0. (b) The predicted variation in the resonant frequency in fluid ω_f with respect to R_0 and T_0. In both panels five curves are shown for T_0=0.5,1, 2, 4, 8. The bounding two curves are labeled with the remaining curves in sequential order. R_0 is evaluated at the resonant frequency of the beam in vacuum. The quality Q is determined by evaluating Eq. (7) at ω_f where ω_f is the frequency that maximizes Eq. (1).

It is typical for $R_0 \sim 1$ and $T_0 \sim 1$ for many proposed microscale applications in water. In this case the analytics predict strongly damped dynamics with $Q \sim 2$. For applications that require a distinct peak to be measured this presents a significant challenge.

Using Euler-Bernoulli beam theory [25] for a doubly clamped beam these expressions can be written as a function of geometry (L,w,h) which are often the experimentally relevant parameters rather than R_0 and T_0. The relevant expressions are

$$\omega_0 = \frac{11.2}{\sqrt{3}} \sqrt{\frac{E}{\rho_b}} \frac{h}{L^2}, \tag{8}$$

$$k = 16E\left(\frac{h}{L}\right)^3 w, \tag{9}$$

$$R_0 = \frac{2.8}{\sqrt{3}} \frac{1}{\nu} \sqrt{\frac{E}{\rho_b}} \left(\frac{w}{L}\right)^2 h, \tag{10}$$

where E is Young's modulus. These expressions for T_0 and R_0 together with Fig. 2 suggest that Q and ω_f increase by reducing the length, increasing the width, or increasing the height of the beam. However, the precise improvement is not clear since the available theoretical predictions are only for long and slender beams. In light of this we have performed full time-dependent and three-dimensional finite element numerical simulations [26] of a wide range of geometries to determine precisely the stochastic dynamics.

B. Numerical approach

To compute the stochastic dynamics of the beams we use the approach discussed in Refs. [5,14] and provide only the essential details necessary for our discussion. The autocorrelation of equilibrium fluctuations in beam displacement are given by the deterministic ring down of the beam to the removal of a point step force applied at $x=L/2$ given by

$$F(t) = \begin{cases} F_0 & \text{for } t \leq 0 \\ 0 & \text{for } t > 0, \end{cases} \tag{11}$$

where t is time and F_0 is the magnitude of the force. The value of F_0 is chosen for each simulation such that the beam deflections remain small and, in this case, the results are independent of its specific value. The autocorrelation of equilibrium fluctuations in beam displacement is then given by

$$\langle z_1(0) z_1(t) \rangle = k_B T \frac{Z_1(t)}{F_0}. \tag{12}$$

We use lower case z_1 to indicate stochastic displacement, and upper case Z_1 to indicate the deterministic ring-down measured at the center of the beam $x=L/2$. The noise spectrum of fluctuations in beam displacement is given by

$$G(\omega) = 4 \int_0^\infty \langle z_1(t) z_1(0) \rangle \cos(\omega t) dt. \tag{13}$$

The noise spectrum is used to determine ω_f and Q for the numerical results. The resonant frequency ω_f is the frequency maximizing $G(\omega)$ and the quality is given by

$$Q \approx \frac{m_f(\omega_f)\omega_f}{\gamma_f(\omega_f)} = \frac{k}{4k_B T} \omega_f G(\omega_f). \tag{14}$$

The right-hand side of Eq. (14) is found using $m_f(\omega_f) = k/\omega_f^2$ and using the peak value of the noise spectrum $G(\omega_f)$ to determine the damping. The error in using the bulk mode spring constant, as opposed to the dynamic spring constant for the fundamental mode, is small and on the order of several percent.

In summary, the numerical procedure is the following: (i) compute $Z(t)$ from a deterministic simulation of the ring down of the beam due to the removal of a step force; (ii) compute the autocorrelation of equilibrium fluctuations in displacement using Eq. (12); (iii) compute the noise spectrum using Eq. (13); (iv) calculate diagnostics: ω_f is the frequency that maximizes the noise spectrum, and Q is found from Eq. (14).

We have performed extensive numerical tests on doubly clamped beams in vacuum and in fluid to ensure the accuracy of our calculations [27]. For each geometry explored we have conducted numerical simulations over a range of spatial and temporal discretizations to ensure the convergence of our reported values for the quality factor and resonant frequency of the fundamental mode in fluid. The required spatial resolution depended significantly upon the geometry explored with the short and wide beam geometries requiring higher spatial resolution. Typically, we found that a time step $\Delta t \leq P/15$ was sufficient where P is the period of the fundamental mode in vacuum. We have also been careful to choose the size of the overall simulation domain to be large enough such that the bounding walls do not affect the results. In our results, the bounding walls are always a distance of $15\delta_s$ or greater from the beam surface where $\delta_s = (\nu/\omega_f)^{1/2}$ is the Stokes length for the fundamental mode in fluid.

TABLE I. The eight geometries of doubly clamped beams used in the numerical simulations. Case (1) is the baseline geometry and the remaining cases are variations of this geometry. The beam aspect ratios are L/w, L/h, and w/h. Cases (2)–(3) are variations in width, cases (4)–(5) are variations in height, and cases (6)–(8) are variations in length. The beams are composed of silicon with Young's modulus $E=210$ GPa, density $\rho_b=3100$ kg/m^3, and the fluid is water with $\rho_f=997$ kg/m^3, $\eta=8.56\times10^{-4}$ kg/ms. All simulations are performed at room temperature with $T=300$ K.

Case	L (μm)	w (μm)	h (μm)	L/w	L/h	w/h
(1)	15	0.4	0.1	37.5	150	4
(2)	15	0.8	0.1	18.75	150	8
(3)	15	1.2	0.1	12.5	150	12
(4)	15	0.4	0.2	37.5	75	2
(5)	15	0.4	0.3	37.5	50	1.33
(6)	5	0.4	0.1	12.5	50	4
(7)	1	0.4	0.1	2.5	10	4
(8)	0.4	0.4	0.1	1	4	4

C. Results

As the baseline geometry we consider a doubly clamped beam with length $L'=15$ μm, width $w'=0.4$ μm, and height $h'=0.1$ μm. This geometry is similar to what has been recently used in experiments demonstrating thermoelastic actuation in vacuum and air [1]. Here, we are interested in the beam dynamics in a viscous fluid and use water. This geometry is referred to as case (1) in Table I and we consider seven additional geometries which are chosen as systematic variations in the baseline geometry (L',w',h'). Also shown in Table I are the aspect ratios for the different geometries to give an idea of the range of geometries used and also to give some indication of the deviation from the ideal case of a long and thin beam used in analytical predictions.

Table II illustrates the deviations in geometry when compared with the baseline geometry of case 1. Also included are the beam properties that can be determined independent of the fluid dynamics which include the bulk spring constant k, the frequency parameter in vacuum R_0, and the mass loading parameter T_0. We have used finite element numerical simulations of the beams in vacuum to determine the numerical values of k and ω_0 for all of the geometries considered. Given this information one can use the analytical expressions to predict Q and ω_f which is illustrated in Fig. 2. From Table II it is clear that over 4 orders of magnitude of spring constant, over 3 orders of magnitude of frequency parameter, and over 1 order of magnitude of the mass loading parameter are considered by the chosen variations in geometry.

We first quantify the stochastic dynamics of the baseline geometry. The numerical results for the autocorrelation of equilibrium fluctuations in beam displacement are shown in Fig. 3(a), and the noise spectrum is shown in Fig. 3(b). In each figure the baseline geometry is labeled w'.

The autocorrelation curves are normalized using k/k_BT where the value of k for each case is given in Table II. The noise spectra have been normalized using the peak value $G(\omega_f)$. These figures illustrate that the dynamics of this micron-scale beam in water are strongly damped. The value of the quality and resonant frequency in fluid using our nu-

TABLE II. The geometry variations with respect to the baseline geometry given by case (1) with (L',w',h'). Cases (2) and (3) explore increasing width, cases (4) and (5) explore increasing thickness, and cases (6)–(8) explore decreasing length. Also shown are the spring constant k, the frequency based Reynolds number in vacuum R_0, and the mass loading parameter T_0. The values of k and R_0 are determined using finite element simulations.

Case	L/L'	w/w'	h/h'	k (N/m)	R_0	T_0
(1)	1	1	1	0.40	1.08	1.01
(2)	1	2	1	0.83	4.55	2.02
(3)	1	3	1	1.21	10.19	3.03
(4)	1	1	2	3.19	2.17	0.51
(5)	1	1	3	10.82	3.19	0.34
(6)	1/3	1	1	10.92	10.20	1.01
(7)	1/15	1	1	1178.95	231.55	1.01
(8)	1/37.5	1	1	11413.04	1146.08	1.01

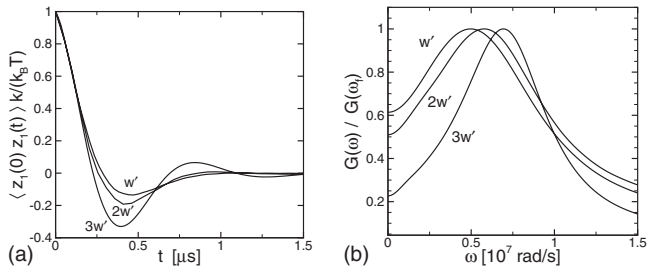

FIG. 3. The autocorrelations and noise spectra of equilibrium fluctuations in beam displacement as a function of beam width from numerical results: case 1 (w'), case 2 ($2w'$), case 3 ($3w'$). (a) The autocorrelations, the results have been normalized using $k/(k_BT)$ for each case. (b) The noise spectra, the results have been normalized by the peak value for each case, $G(\omega_f)$.

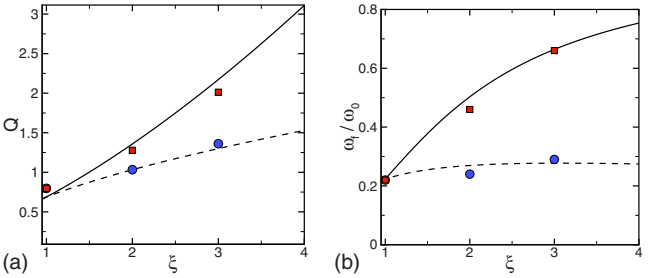

FIG. 4. (Color online) Comparison of numerical results with analytical predictions for Q and ω_f as a function of width w and height h. The circles (blue) are for increasing width and the squares (red) are for increasing height. The solid line is the analytical prediction for increasing width and the dashed line is the analytical prediction for increasing height. To place all values on a single plot $\xi=w/w'$ for the varying width results and $\xi=h/h'$ for the varying height results.

merical results are given in Table III and are $Q=0.80$ and $\omega_f/\omega_0=0.22$. Also shown are the predictions from analytics using Eqs. (1) and (7) which yield $Q^\dagger=0.68$ and $\omega_f/\omega_0^\dagger=0.22$. The analytical predictions are quite accurate for the frequency drop while under predicting the quality factor for this geometry.

Next we consider the variation in the stochastic dynamics of the beam as a function of the beam width. In particular, we double and triple the beam width w while holding L and h constant. For increasing width the frequency parameter increases as $R_0\sim w^2$ while the mass loading parameter increases as $T_0\sim w$. This has the effect of increasing the fluid inertia while simultaneously increasing the mass loading. These two counteracting effects suggest the increase in Q and ω_f will only be moderate. The autocorrelations and noise spectra from numerical simulations are shown in Fig. 3. The autocorrelation results exhibit both positively and negatively correlated results as expected with the dynamics becoming more underdamped as the width is increased. The noise spectra clearly illustrate that the peak value shifts to higher frequency and that the peak itself becomes sharper as the width increases. For case 1, the noise spectra have significant contributions at low frequency whereas for case 3 the noise spectra have become more symmetric with a Lorentzian shape.

Values for the quality and resonant frequency in fluid from our numerical results are given in Table III. When compared to the quality for the baseline geometry Q', the increase in quality is $Q/Q'=1.29$ for doubling the width, and $Q/Q'=1.71$ for tripling the width. The quality increases with increasing width however the magnitude of the quality is small indicating that the beam dynamics remains strongly damped. The increase in the value of ω_f/ω_0 is slightly less than what is found for Q. A comparison of our numerical values of ω_f and Q with the analytical predictions of Eqs. (1) and (7) is shown in Fig. 4. The circles are the results from our numerical simulations and the dashed line is the analytical prediction where $\xi=w/w'$ and w' is the width of the baseline geometry. It is clear that the analytical predictions remain quite accurate over this range. This includes case 3 where $L/w\approx w/h\approx 12$ and $L/h\gg 1$. Figure 4 indicates that the magnitude of the increase in quality with increasing width is quite moderate. Furthermore, the increase in ω_f is quite small and becomes nearly flat at $\omega_f/\omega_0\approx 0.24$ for $\xi\gtrsim 2$.

Next we consider the variation in beam dynamics as the height is increased. We consider the cases where h is doubled and tripled while the L and w are held constant. As the height is increased the frequency parameter increases as $R_0\sim h$ whereas the mass loading parameter decreases as $T_0\sim h^{-1}$. These two effects both contribute to increasing Q and ω_f.

TABLE III. The stochastic dynamics of the beams in fluid. Shown is the frequency based Reynolds number in fluid R_f, the reduction in the resonant frequency ω_f/ω_0, and the quality factor Q. Also shown is the improvement of the quality with respect to that of case (1) given by $Q'=0.8$. $Q^\dagger$ and $\omega_f/\omega_0^\dagger$ are the results predicted from analytical theory using Eqs. (1) and (7).

Case	R_f	ω_f/ω_0	Q	Q/Q'	$\omega_f/\omega_0^\dagger$	$Q^\dagger$
(1)	0.23	0.22	0.80	1.0	0.22	0.68
(2)	1.08	0.24	1.03	1.29	0.27	1.05
(3)	2.91	0.29	1.36	1.71	0.28	1.31
(4)	1.00	0.46	1.28	1.61	0.50	1.35
(5)	2.11	0.66	2.01	2.52	0.66	2.13
(6)	4.80	0.47	1.57	1.97	0.51	2.04
(7)	164.46	0.71	6.13	7.69	0.67	9.22
(8)	885.19	0.77	5.90	7.40	0.69	20.24

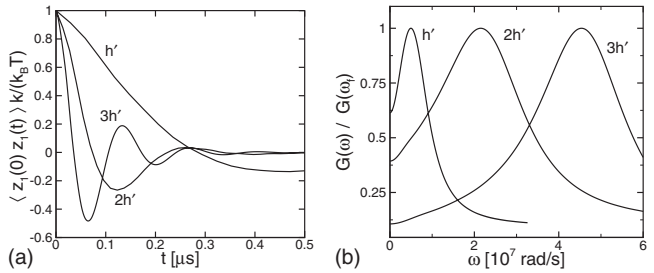

FIG. 5. The autocorrelations and noise spectra as a function of beam height from numerical results: case 1 (h'), case 4 ($2h'$), case 5 ($3h'$). (a) The normalized autocorrelations. (b) The normalized noise spectra.

The normalized autocorrelations and noise spectra from our numerical simulations are shown in Fig. 5. The results clearly indicate an increasing value of both ω_f and Q and numerical values are given in Table III. The relative increase in quality is $Q/Q'=1.61$ when the height is doubled, and $Q/Q'=2.52$ when the height is tripled. The increase in ω_f/ω_0 follows a similar trend.

A comparison of our numerical results with the predictions of theory is shown in Fig. 4 using $\xi=h/h'$. The square symbols are the numerical results and the solid line is the analytical prediction. It is clear that the increases in Q and ω_f are much larger for variations in height when compared to what was found for increases in beam width. The analytical predictions remain quite accurate and insightful over the range of aspect ratios explored by varying the beam height. We highlight that this includes case 5 where $w/h\approx 1$.

The last case we consider is decreasing the beam length while holding the width and height constant. In this case the frequency parameter increases rapidly as $R_0\sim L^{-2}$ whereas T_0 remains constant. The autocorrelations and noise spectra are shown in Fig. 6 which illustrate a significant increase in resonant frequency and quality. From Fig. 6(a) the results for the most extreme geometry explored, $L'/37.5$, clearly show the influence of higher harmonics. The numerical values of Q and ω_f from our numerical results are given Table III. For case 8 where $L/L'=37.5$ the increase in quality is $Q/Q'=7.4$ and the reduction in the resonant frequency when compared to its value in vacuum is $\omega_f/\omega_0=0.77$ indicating significant changes are possible by changing the beam length.

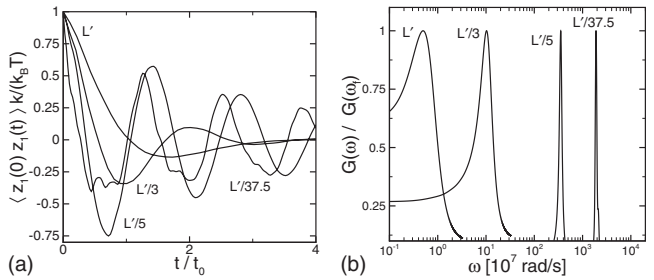

FIG. 6. The autocorrelations and noise spectra as a function of beam length from numerical results: case 1 (L'), case 6 ($L'/3$), case 7 ($L'/5$), case 8 ($L'/37.5$). (a) The normalized autocorrelations. (b) The normalized noise spectra.

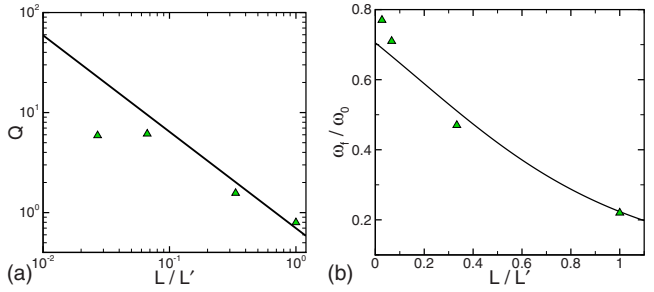

FIG. 7. (Color online) The variation in the quality Q, panel (a), and of the resonant frequency in fluid ω_f/ω_0, panel (b), by decreasing the length L of the beam relative to the value of case (1) given by L'. The triangles are the results from numerical simulation and the solid line is the analytical prediction.

The analytical predictions given in Table III show significant deviations from our numerical results. This is also illustrated in Fig. 7 where the triangles are the numerical results and the solid lines are the analytical predictions. For case 6 ($L/w=12.5$) the analytical predictions are quite accurate. However, for case 7 ($L/w=2.5$) and case 8 ($L/w=1$) the analytical predictions over predict Q and under predict ω_f/ω_0. The approximation of using the fluid flow from an infinite two-dimensional oscillating cylinder is no longer well justified. The numerical results suggest the presence of additional modes of fluid dissipation that are not captured in the two-dimensional theory.

To explore this further we quantify the fluid motion around the beam in the deterministic numerical simulations where the beam rings down upon the removal of a step force. Figures 8 and 9 illustrate the magnitude of the fluid velocity in the transverse u_z and axial u_x directions, respectively. The velocities are plotted along a line beginning at $(0.0,0.0,0.01\ \mu\text{m})$ and ending at $(L,0.0,0.01\ \mu\text{m})$ for all cases. In our notation the fluid velocity in the (x,y,z) directions is (u_x,u_y,u_z), see Fig. 1 for the definition of the coordinate directions (x,y,z). The velocities are shown at the time when the velocity of the beam is at its maximum value which occurs when the center of the beam crosses $z=0$ the first time during its ring down. The maximum value of u_z at

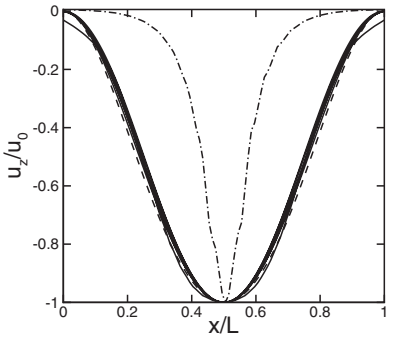

FIG. 8. The transverse fluid velocity u_z for cases 1–8 along the line beginning at $(0.0,0.0,0.01\ \mu\text{m})$ and ending at $(L,0.0,0.01\ \mu\text{m})$ from the deterministic numerical simulations where the beam velocity is at its maximum value. The baseline geometry is shown as the dashed line, cases 2–7 are the solid lines, and case 8 is the dash-dot line.

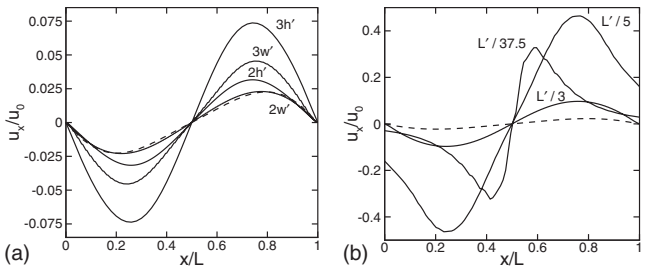

FIG. 9. The normalized axial velocity from numerical simulation. (a) The axial velocity found when varying the width and height of the baseline geometry. (b) The axial velocity found when decreasing the length of the baseline geometry. The results for the baseline geometry are given by the dashed line. The axial velocities are computed along a line in the x direction with origin $(0,0,0.01\ \mu\text{m})$ and end point $(L,0,0.01\ \mu\text{m})$, see Fig. 1 for definitions of coordinate directions. The velocity is normalized by u_0 for each case where u_0 is the maximum transverse velocity which occurs at $x=L/2$. The abscissa is normalized by the length L for each case.

this time is labeled u_0 and is used to normalize both the transverse and axial velocities. The axial direction is normalized by the length so that all cases can be represented on the same figure.

Figure 8 shows the transverse fluid velocity u_z for cases 1–8. The baseline geometry (dashed line) and cases 2–7 (solid lines) collapse onto a single curve with a shape similar to that of the fundamental mode of a doubly clamped beam. Case 8 differs significantly with a much sharper peak indicating that its dynamics are quite different which is expected since this geometry is substantially different than the others.

Figure 9(a) illustrates the normalized axial velocities u_x as the beam width and height are varied. In the approximation of a two-dimensional flow the axial velocity is identically zero and any deviations from this in the numerical results indicate fluid dynamics not considered in the analytical predictions. The bimodal shape of the curves is expected from the symmetry of the fundamental mode. For $x>L/2$ the axial fluid velocity is positive and for $x<L/2$ it is negative. The baseline geometry is shown as the dashed line and has a negligible axial fluid velocity. At its maximum value it is only $\sim 2.5\%$ of the maximum transverse velocity u_0. A similar trend is found for cases 2–5. As the width or height is increased the relative magnitude of the axial velocities increases. It is expected that if larger values of the width or height were computed the axial velocities would become significant and at this point the analytical predictions would show large deviations.

Figure 9(b) shows the relative value of the axial velocities as the length of the beam is decreased. The baseline geometry is included for reference as the dashed line. It is clear that the axial velocities are now quite significant and range from 10% to 40% of u_0. The axial velocities do not vanish at $x=0,L$ for cases 7 and 8 because these beams are held by rigid supports [see Fig. 1] and the lateral side walls of the numerical domain are distant. The axial velocities result in fluid dissipation not accounted for in the two-dimensional theory and contribute significantly to the lower values of Q found in the numerical simulations. Furthermore, ω_f from the numerical simulations is larger than the analytical predictions. The added mass in the simulations is smaller than the predicted values and this reduction is a direct result of the three-dimensionality of the fluid flow. The maximum value of the relative axial velocity does not follow a monotonic trend with L because as the length becomes small the precise nature of the beam dynamics varies in a complicated manner which directly affects the fluid motion and therefore the fluid dissipation. In fact, the smallest beam $L'/37.5$ has an aspect ratio of $L/w=1$ and is better described as a plate undergoing complicated dynamics as indicated by the presence of higher mode effects in Fig. 6(a). Overall, our results suggest that the relative magnitude of the axial velocity can be used to indicate the applicability of the two-dimensional theory.

In many microscale technologies the ability to sense small forces is important and therefore a small spring constant is desirable. In light of this, the improved performance, as measured by increased values of Q and ω_f with increasing w, increasing h, or decreasing L all come at the price of reduced force sensitivity. Using Eq. (9) to estimate k yields its dependence upon geometry and the magnitude of the improved performance follows the same trend as increasing k. Overall, these tradeoffs would need to be balanced in a particular application.

III. CONCLUSIONS

The stochastic dynamics of micron and nanoscale elastic beams can be directly quantified using deterministic numerical computations for the precise geometries and conditions of experiment. We have shown that the geometry of doubly clamped beams can be tailored to overcome the strong fluid damping that occurs for small scale systems in a viscous fluid. Our numerical exploration has been used to build physical insights into the stochastic dynamics and to place realistic bounds upon the applicability of the two-dimensional theory. Overall, we find that the two-dimensional theory is quite accurate far beyond what may have been expected based upon the underlying assumptions. When deviations do occur a significant factor is fluid velocities in the axial direction resulting in increased dissipation and a lower added mass. It is anticipated that these results will be useful in guiding the development of future experiments by providing the basis for predictions that cover a wide range of geometries. Furthermore, our results provide insight into the development of accurate theoretical models valid for the finite geometries used in experiment.

ACKNOWLEDGMENTS

This research was funded by AFOSR Grant No. FA9550-07-1-0222. Partial support was also provided by NSF REU Grant No. DMR-0552661 and a Virginia Tech ASPIRES grant. We would also like to acknowledge many useful interactions with Matt Clark, Carlos Carvajal, Michael Roukes, Jessica Arlett, and Igor Bargatin.

[1] I. Bargatin, I. Kozinsky, and M. Roukes, Appl. Phys. Lett. **90**, 093116 (2007).
[2] S. Verbridge, L. Bellan, J. Parpia, and H. Craighead, Nano Lett. **6**, 2109 (2006).
[3] R. Garcia and R. Perez, Surf. Sci. Rep. **47**, 197 (2002).
[4] K. L. Ekinci and M. L. Roukes, Rev. Sci. Instrum. **76**, 061101 (2005).
[5] M. R. Paul and M. C. Cross, Phys. Rev. Lett. **92**, 235501 (2004).
[6] A. Maali, C. Hurth, R. Boisgard, C. Jai, T. Cohen-Bouhacina, and J. Aime, J. Appl. Phys. **97**, 074907 (2005).
[7] T. Braun, V. Barwich, M. K. Ghatkesar, A. H. Bredekamp, C. Gerber, M. Hegner, and H. P. Lang, Phys. Rev. E **72**, 031907 (2005).
[8] M. Ghatkesar, T. Braun, V. Barwich, J. Ramseyer, C. Gerber, M. Hegner, and H. P. Lang, Appl. Phys. Lett. **92**, 043106 (2008).
[9] R. Stark, T. Drobek, and W. Heckl, Ultramicroscopy **86**, 207 (2001).
[10] S. Basak, A. Raman, and S. Garimella, J. Appl. Phys. **99**, 114906 (2006).
[11] J. Tamayo, A. D. L. Humphris, R. J. Owen, and M. J. Miles, Biophys. J. **81**, 526 (2001).
[12] L. Sekaric, M. Zalalutdinov, R. Bhiladvala, A. Zehnder, J. Parpia, and H. Craighead, Appl. Phys. Lett. **81**, 2641 (2002).
[13] T. P. Burg, M. Godin, S. M. Knudsen, W. Shen, G. Carlson, J. S. Foster, K. Babcock, and S. R. Manalis, Nature **446**, 1066 (2007).
[14] M. R. Paul, M. T. Clark, and M. C. Cross, Nanotechnology **17**, 4502 (2006).
[15] M. R. Paul and J. E. Solomon, *Nanodevices for Life Sciences* (Weinheim, Germany, 2005), Vol. 4, Chap. 1.
[16] R. J. Clarke, O. E. Jensen, J. Billingham, A. P. Pearson, and P. M. Williams, Phys. Rev. Lett. **96**, 050801 (2006).
[17] R. J. Clarke, S. M. Cox, P. M. Williams, and O. E. Jensen, J. Fluid Mech. **545**, 397 (2005).
[18] M. T. Clark and M. R. Paul, Int. J. Non-Linear Mech. **42**, 690 (2007).
[19] E. O. Tuck, J. Eng. Math. **3**, 29 (1969).
[20] J. E. Sader, J. Appl. Phys. **84**, 64 (1998).
[21] C. Van Eysden and J. E. Sader, Phys. Fluids **18**, 123102 (2006).
[22] R. J. Clarke, O. E. Jensen, J. Billingham, and P. M. Williams, Proc. R. Soc. London, Ser. A **462**, 913 (2006).
[23] G. G. Stokes, Trans. Cambridge Philos. Soc. **9**, 8 (1851).
[24] L. Rosenhead, *Laminar Boundary Layers* (Oxford University Press, New York, 1963).
[25] L. D. Landau and E. M. Lifshitz, *Theory of Elasticity* (Butterworth-Heinemann, Oxford, England, 1959).
[26] ESI CFD Headquarters, Huntsville AL 25806. We use the CFD-ACE+solver.
[27] M. Villa, Master's thesis, Virginia Polytechnic Institute and State University, June 2009.